Practical method for calculation of multiple light scattering

Arthur E. Bailey and David S. Cannell
Physics Department, University of California, Santa Barbara, California 93106
(Received 16 February 1994)

We present a method for directly simulating multiple light scattering to all orders. This method is quite general and should be adaptable for use with any optical geometry. It has been tested by using the simulation to calculate the amount of multiple scattering and to correct light scattering data for a critical binary fluid mixture near its consolute point in a standard scattering geometry that rejects most multiple scattering. Such geometries make simulation difficult since very few simulated scattering events are accepted by the optics. We also present, as an example of the flexibility of the method, an analysis of multiple scattering from a critical binary fluid mixture undergoing phase separation in a very different optical geometry which does not reject multiple scattering.

PACS number(s): 78.35.+c, 42.25.Fx, 64.60.Fr

I. INTRODUCTION

Multiple scattering limits the usefulness of scattering techniques for samples that scatter very strongly. It occurs commonly in light scattering from concentrated suspensions and from samples near critical points. Multiple scattering is not limited to light scattering, but can be problematic in the scattering of any probe. The presence of the additional scattering affects the measurement of both the angular distribution and the absolute intensity of the scattering. Since the angular distribution determines the basic length scale of the fluctuations responsible for the scattering, while the intensity determines their mean-squared amplitude, such distortions can have serious consequences for data interpretation. Throughout this paper the term multiple scattering will be used to refer to photons that have been scattered out of the beam and then scattered one or more additional times before exiting the cell, while single scattering will refer to photons that were scattered out of the beam, but underwent no further scattering before exiting the cell.

Several attempts have been made to calculate the intensity of double scattering for various scattering geometries [1–5]. Perhaps the most useful of these is that of Shanks and Sengers, which reduces the six-dimensional integral for the double scattered intensity to a double integral for a realistic light scattering geometry. Unfortunately, the method applies only to a particular form of the scattering cross section, namely, the Ornstein-Zernike (OZ) form observed near critical points. The method can be generalized to cross sections of the Fisher-Burford type [6], but not to arbitrary cross sections. Furthermore, a correction to all orders of multiple scattering is needed since there are few circumstances where double scattering is important and higher orders are not. The direct approach of expressing multiply scattered intensities as many-fold integrals (sixfold for double scattering, ninefold for triple scattering, etc.) rapidly becomes very complicated.

Under conditions of strong multiple scattering, direct simulation of the scattering process by launching photons and using a Monte Carlo approach to propagate them from one scattering event to the next is very appealing. This approach has been used to simulate multiple Compton scattering [7–9], but it is not very practical for typical light scattering geometries because they strongly reject photons which do not appear to come from a very limited region at the center of the cell and scatter into a small, well defined solid angle. These geometries are designed precisely so as to minimize both multiple scattering and stray elastically scattered light generated by repeated scattering from surfaces. For such a geometry nearly every simulated photon is rejected by the optics once it has been laboriously propagated through the sample; however, this problem can be overcome by employing a simple artifice. We imagine an instrument that has scattering channels with the desired optical geometry covering the entire 4π sr of solid angle, as opposed to the $\sim 10^{-4}$ sr per scattering channel actually subtended by a typical instrument. This results in accurate statistics for multiple scattering, even after restricting scattering events to those which appear to come from a well defined region of the cell. The ratio of multiple scattering to single scattering as a function of direction can then be fit to a smooth function. Averaging this function over the acceptance solid angles of the actual experimental scattering channels yields the desired result: the ratio of multiple to single scattering for the scattering cross section and geometry of interest.

To correct experimental data for the effects of multiple scattering an iterative approach is used to determine the single scattering from the measured total scattered intensity. Starting from an initial estimate of the scattering cross section, the simulation is repeatedly used to deduce improved estimates until the estimated cross section yields a total scattered intensity which agrees with the uncorrected experimental data for all measured scattering angles. Clearly, there is no guarantee that such a process must converge or that a unique single scattering cross section corresponds to a given experimental data set. In practice, however, the process is robust and has yielded reasonable results.

The measured integrated scattering cross section or turbidity τ has proved to be extremely useful. It can be obtained accurately from the transmitted beam power, which is attenuated only by single scattering. The constraint placed on the cross section by τ is quite strong and is useful in the process of deducing the single scattering cross section in the presence of multiple scattering. To be precise, we should point out that we refer to the Rayleigh factor, the differential scattering cross section per unit volume of sample, as the scattering "cross section."

Section II details the methods used to propagate the photons through the cell. The photons exiting the cell must pass the criteria for acceptability and then the ratio of acceptable multiply scattered intensity to singly scattered intensity as a function of scattering angle must be fit to a smooth function; the methods used to do this are described in Sec. III. In Sec. IV the simulation is used to correct data from two very different experimental scattering cross sections and geometries: scattering from a critical binary fluid mixture near its consolute point and a different binary fluid mixture undergoing phase separation. Section V is a discussion of this method of calculating multiple scattering, its limitations, and possible generalizations.

II. LAUNCHING AND PROPAGATION OF PHOTONS

For simplicity, the incident beam is considered to be linearly polarized and single scattering to be perfectly polarized. For computational efficiency, only photons that are scattered while traversing the cell are tracked. The incident beam is taken to be a line source (which is not necessary) and is divided into sections, each of which contributes the same number of initial scattering events. The various possible scattering directions are binned into elements of solid angle so that each direction is equally likely for a scattering event. This assumes knowledge of the single scattering cross section and, consequently, the process of correcting data is necessarily iterative. This section describes in detail how the incident beam is divided, how the bins are chosen for different scattering directions, and how the photons are propagated within the cell.

Due to scattering, the optical power in the incident beam falls off with x, the distance traveled in the sample, as $P(x) = P_0 e^{-\tau x}$, where τ is the turbidity in cm^{-1}. The number of photons that are scattered out of the beam between x_1 and x_2 is given by

$$\Delta N(x_1, x_2) = N_0[e^{-\tau x_1} - e^{-\tau x_2}], \tag{2.1}$$

where N_0 is the number incident on the sample over the course of the measurement. With a beam of total length $2R$ in the sample the total number scattered will be $N_0(1 - e^{-2\tau R})$. If it is to be divided into M sections, each of which scatters the same number of photons, then we must have

$$\frac{1 - e^{-2\tau R}}{M} = (e^{-\tau x_i} - e^{-\tau x_{i+1}}), \tag{2.2}$$

where the ith beam segment lies between x_{i-1} and x_i, with $x_0 = 0$. This set of equations is easily solved for the x_i and the photons are then launched from the centers of each section.

Since τ^{-1} sets a natural length scale for the problem, one might be tempted to use about ten sections per τ^{-1}. For optical collection geometries that do not discriminate against photons based on where they appear to originate, this is probably acceptable. For geometries that discriminate heavily, however, more care is required. For example, a common scheme is to image the scattered light onto a small slit or aperture, thus accepting light from a sample only if it comes from (or appears to come from) a small portion of the incident beam which may be less than 0.01 cm long. In this case, it is necessary to increase the number of beam sections until the length of the sections is less than the width of the slit image in the cell. We typically used at least 250 sections per centimeter.

It is desirable to bin (assign solid angle increments to) the possible scattering directions in a manner that results in the same scattering probability per bin. This allows photons to be propagated in a very efficient manner for a given scattering cross section. In principle one could choose the increments of solid angle using spherical polar coordinates with the z axis parallel to the direction of propagation of the incident beam. In this case the polar angle θ is the scattering angle and the increment of solid angle is given by $\Delta\Omega \simeq \sin\theta\,\Delta\theta\,\Delta\varphi$. This binning scheme suffers from the problem that for values of θ near 0° and 180° very large increments in θ and/or φ are required to achieve a reasonable value for $\Delta\Omega$. In scattering geometries where the instrument includes channels at small and/or large θ, one cannot tolerate such large bins as they distort the distribution significantly near $\theta = 0°$ and 180°. We solved this problem for a geometry that includes a channel at $\theta = 2.7°$ (that of Haller *et al.* [10]) by binning in terms of spherical polar coordinates with the z axis oriented along the direction of polarization of the incident photons, as shown in Fig. 1. In this case the troublesome directions are located well away from

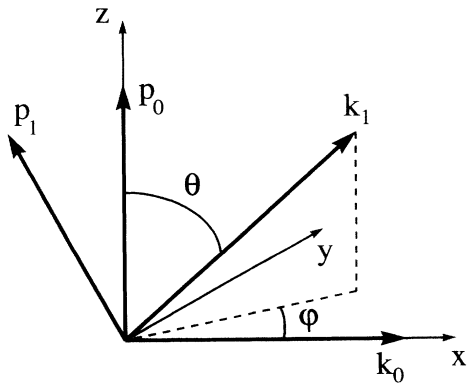

FIG. 1. Coordinate system used in the simulation. The beam is incident along the x axis and polarized along the z axis. A photon scattered in the direction $\hat{k}_1$ is polarized in the direction $\hat{p}_1$. The scattering angle is the angle between $\hat{k}_1$ and the x axis, while the polar angle θ is the angle between the incident polarization and the scattered wave vector k_1.

the x-y plane, where the detectors are located in many typical scattering geometries. We will use this system of coordinates throughout the remainder of this paper.

The scattering cross sections of interest have the form

$$\frac{d\sigma}{d\Omega}(\theta,\varphi) = f(q)\,\sin^2\theta, \tag{2.3}$$

where the scattering wave vector q is given by

$$q = \frac{4\pi n}{\lambda_0}\left(\frac{1-\sin\theta\,\cos\varphi}{2}\right)^{1/2}, \tag{2.4}$$

with n the sample refractive index and λ_0 the vacuum wavelength. Since the cross section is symmetric about $\theta = \frac{\pi}{2}$ and about $\varphi = 0$, we only need bin the region $0 \le \theta \le \frac{\pi}{2}$, $0 \le \varphi \le \pi$. The scheme employed is indicated schematically in Fig. 2.

The unit sphere is divided into bands as shown in Fig. 2, with each band having a given width in θ independent of φ. We allowed the width of the bands to increase and the number of bins within each band to decrease as θ decreased so that the linear dimensions (on the unit sphere) of the average bin within each band remained equal in both the θ and φ directions. Since each bin is to correspond to the same scattering probability, the extent of the bins in the φ direction within a given band must vary inversely with the scattering cross section, as indicated schematically in the figure.

The binning process began at $\theta = \frac{\pi}{2}$, using bands of the form $\theta_{i+1} \le \theta \le \theta_i$ with $\theta_0 = \frac{\pi}{2}$ and $\theta_1 = \frac{\pi}{2} - \frac{\pi}{360}$, typically. This first band was then divided into 360 bins over the range $0 \le \varphi \le \pi$. The integrated cross section per bin σ_0 was determined by numerically integrating the cross section over the first band:

$$\sigma_0 = \frac{1}{360}\int_0^{\pi}\int_{\frac{\pi}{2}-\frac{\pi}{360}}^{\frac{\pi}{2}} \frac{d\sigma}{d\Omega}\,\sin\theta\,d\theta\,d\varphi. \tag{2.5}$$

The values of φ corresponding to each of the bins in this band were then found by solving the equations

$$\sigma_0 = \int_{\varphi_{n-1}}^{\varphi_n}\int_{\frac{\pi}{2}-\frac{\pi}{360}}^{\frac{\pi}{2}} \frac{d\sigma}{d\Omega}\,\sin\theta\,d\theta\,d\varphi \tag{2.6}$$

for the φ_n, $n = 1, 2, \ldots, 360$, with $\varphi_0 = 0$.

Having binned the first band, the angular width of the second band in the θ direction could then be determined. Keeping the linear extent of the average bin in the θ and φ directions equal requires $\sin\bar{\theta}\,\overline{\Delta\varphi} \simeq \Delta\theta$, where an overbar denotes an average value. Thus the number of bins in any particular band $\pi/\overline{\Delta\varphi}$, can be written $\pi\,\sin\bar{\theta}/\Delta\theta$ and the angular extent $\Delta\theta_i$ of the ith band in the θ direction can be estimated by numerically solving the equation

$$\frac{\sigma_0\pi\,\sin\bar{\theta}_i}{\Delta\theta_i} = \int_0^{\pi}\int_{\theta_i-\Delta\theta_i}^{\theta_i} \frac{d\sigma}{d\Omega}\,\sin\theta\,d\theta\,d\varphi \tag{2.7}$$

for $\Delta\theta_i$. The number of bins was obtained by truncating the quantity $\pi\,\sin\bar{\theta}_i/\Delta\theta_i$ to an integer n_i. With n_i fixed, the equation

$$n_i\sigma_0 = \int_0^{\pi}\int_{\theta_i-\Delta\theta_i}^{\theta_i} \frac{d\sigma}{d\Omega}\,\sin\theta\,d\theta\,d\varphi \tag{2.8}$$

was finally solved for $\Delta\theta_i$. This band was then divided into n_i bins in the φ direction as before and the process repeated until binning was completed. This typically generated about 60 000 bins and required ~10 min on a NeXT workstation.

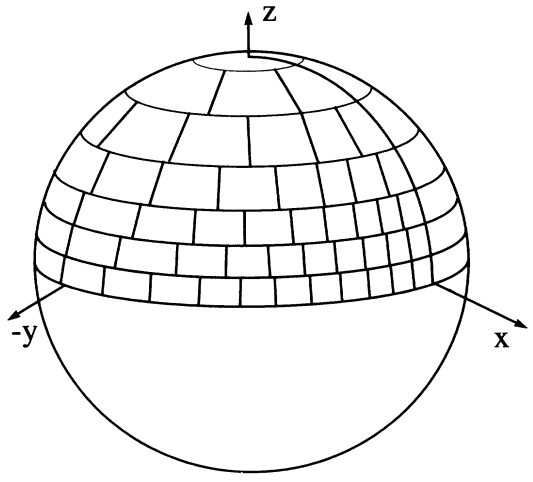

FIG. 2. Schematic diagram of the equal scattering probability bins associated with different scattering directions. The bins are arranged in bands, each of which subtends a small angular range in the polar direction. The bins within each band vary in their extent in the azimuthal direction, and the bands vary in their extent in the polar direction, in such a manner that each bin corresponds to the same scattering probability. The bands vary in their polar extent and in the number of bins each contains so as to have the average dimensions (on the unit sphere) of the bins within a given band equal in both the polar and azimuthal directions.

The result of the binning procedure is a look-up table containing unit vectors $\hat{k}_i$ corresponding to the direction of the center of each bin, as well as unit vectors $\hat{p}_i$ giving the direction of polarization for photons scattered into each of the bins, i.e., the polarization vectors for single scattered photons in the geometry of Fig. 1. In addition it is useful to store the vectors $\hat{p}_i \times \hat{k}_i$.

Photons are launched from the centers of the beam sections, an equal number directed at the center of each of the bins. The probability that a photon will be rescattered before it reaches the limit of the sample, a cell wall or a meniscus, a distance d along its direction of travel is $1 - e^{-\tau d}$. A random number determines whether the photon is rescattered or exits. If it is rescattered, another random number m, uniformly distributed between 0 and 1, is chosen to determine where it rescatters. The photon is taken to rescatter at a point a distance l along its direction of travel such that the probability that it will be scattered within that distance $1 - e^{-\tau l}$ is given by $m(1 - e^{-\tau d})$. In other words, m is taken as the conditional probability that it will rescatter within a distance l, given that it will rescatter before exiting the sample. The distance to the rescattering event is then given by

$$l(m) = -\frac{1}{\tau}\ln[1 - m(1 - e^{-\tau d})]. \quad (2.9)$$

A third random number is chosen, multiplied by the total number of directional bins and truncated to an integer to choose the scattering direction. The rescattering is done in a reference frame in which the photon was traveling in the x' direction and was polarized in the z' direction before rescattering. The final step is to transform the new direction of travel and polarization back to the fixed frame from the primed frame. This is done using

$$\begin{pmatrix} \hat{k}_x & (\hat{p}\times\hat{k})_x & \hat{p}_x \\ \hat{k}_y & (\hat{p}\times\hat{k})_y & \hat{p}_y \\ \hat{k}_z & (\hat{p}\times\hat{k})_z & \hat{p}_z \end{pmatrix} \begin{pmatrix} v'_x \\ v'_y \\ v'_z \end{pmatrix} = \begin{pmatrix} v_x \\ v_y \\ v_z \end{pmatrix} \quad (2.10)$$

for any vector $\vec{v}$. Here the $\hat{k}_i$ are the components of the unit vector $\hat{k} = \hat{x}'$, giving the direction of propagation before rescattering, the $\hat{p}_i$ are the components of the unit vector $\hat{p} = \hat{z}'$, giving its polarization before rescattering, and $\hat{p}\times\hat{k}$ is $\hat{y}'$. Thus all of the elements of the transformation matrix are stored in the look-up table. The directions of propagation $\hat{k}'$ and polarization $\hat{p}'$ in the primed frame are simply those stored in the look-up table at the location corresponding to the rescattering direction. The transformation is applied to these vectors and the results become the new values of $\hat{p}$ and $\hat{k}$ for the photon.

Knowing the launch coordinates (location at which the photon rescattered), the wave vector, and the polarization of the rescattered photon, the entire process is repeated until the photon exits the sample. This is continued until the same number of photons has been launched into all possible scattering directions from each section of the incident beam. The result of tracking the photons through the sample is a stream of final launch coordinates, wave vectors, and polarizations of all exiting photons. Refractive corrections were not applied to exiting photons since the ratio of multiple scattering to single scattering is not affected for the geometries studied here, but very little extra computer time would be required to do so.

III. ANALYSIS OF EXITING PHOTONS

A. Acceptance criteria

The result of the simulation described above is a stream of the locations and directions for which scattered photons exited the sample. Information on single scattered photons was eliminated to yield a list of locations and directions for multiply scattered photons only. Not all of these will be detected by the experimental apparatus; the constraints of the scattering geometry must be applied to the exiting photons. Most apparatus detect either very little of the scattered light or nearly all of it. Optical arrangements that reject multiple scattering make the corrections more difficult to calculate since nearly all of the photons that are tracked through the sample are rejected.

Our solution to this problem is to use as much of the information conveyed by the list of exiting multiply scattered photons as possible. Consider, for example, the apparatus described by Haller *et al.* [10]. In this apparatus, the sample is placed in the center of a circular bath of flowing water. The incident laser beam passes through the cylindrical cell along a diameter. The light scattered into a small solid angle is detected at 18 fixed scattering angles by placing an apertured lens for each angle in the wall of the bath. Each lens images the center of the cell onto a slit oriented perpendicular to the image of the beam within the cell. An optical fiber leading to a photomultiplier tube is placed directly behind each slit. The slit is narrow compared to the length of the image of the beam in the cell; therefore, for each scattering channel only light that appears to come from a small region centered in the cell and that has been scattered into a small element of solid angle is accepted. Since both criteria must be satisfied simultaneously, the number of acceptable paths that multiply scattered photons can follow is very restricted, leading to extremely poor statistics. One solution to this problem is to imagine that there is a set of virtual collection optics oriented with its axis parallel to the direction of travel of each exiting photon and imaging the center of the cell onto a virtual slit. Photons that are acceptable to these virtual channels form a distribution in θ and φ that can be fit to a smooth function of these variables. As an example, using virtual slits of width 0.1 mm for a cylindrical scattering cell of diameter 17.2 mm resulted in 0.1% of the photons launched leading to acceptable multiply scattered photons for a particular scattering cross section we studied. Without the use of virtual channels almost no acceptable events would have been generated.

As with the experimental apparatus, the virtual channel is imagined to consist of a lens and a slit placed directly in front of a 1-mm-diam optical fiber. The slit and fiber together define a nearly rectangular field stop whose width is the slit width and long dimension (height) is the diameter of the optical fiber. The virtual slit relevant to an exiting photon is oriented with its long axis perpendicular to the plane containing both the wave vector of the exiting photon and that of the incident beam. The plane in which the slit lies is taken to be normal to the wave vector of the exiting photon. The lens images this rectangular stop in the center of the cell and the photon must appear to have come from this image to be acceptable.

The final point of scattering $\vec{r}$ and direction $\hat{k}$ of the exiting photon determines where the photon appears to have crossed the plane in which the image of the field stop lies. It is convenient to define a coordinate system with its origin at the center of the cell, which is denoted by the subscript a. The $\hat{x}_a$ axis is chosen parallel to the wave vector of the exiting photon. The $\hat{z}_a$ axis, which is the long axis of the stop, is chosen to be $\hat{z}_a = (\hat{k}\times\hat{x})/|\hat{k}\times\hat{x}|$. The point in this plane from which the photon appears to come $(0, y_{ap}, z_{ap})$ has coordinates $y_{ap} = \hat{y}_a \cdot \vec{r}$ and $z_{ap} = \hat{z}_a \cdot \vec{r}$. The criterion for acceptance is then simply

$|\hat{y}_a \cdot \vec{r}| \leq$ (stop image width/2) and $|\hat{z}_a \cdot \vec{r}| \leq$ (stop image height/2).

B. Fitting

In order to fit the acceptable photons to a smooth distribution function, the numbers of acceptable photons that arrive in suitably chosen increments of solid angle were counted. Since the exiting photons consist of a long list of values for θ and φ, it is convenient to choose a simple square grid in θ and φ for the increments. The grid should be coarse enough to contain a reasonable number of photons per increment and small enough to avoid excessive smearing of the photon distribution. A grid 1° on a side has worked well for the simulations described here.

The only problem encountered in binning the exiting photons into this new grid resulted from the fact that the bands of solid angle bins used in the original simulation in a range around $\theta = \frac{\pi}{2}$, which is the region of greatest interest, are very nearly the same size in the θ direction, resulting in many double scattered photons exiting along paths with nearly identical θ values. If a photon is initially launched into the center of a bin in the band closest to $\theta = \frac{\pi}{2}$ and then rescatters into the center of a bin in the same band, it will exit with a θ value equal to the value of the width of that band. Thus doubly scattered photons tend to artificially accumulate along lines of constant θ which are integer multiples of the width of the bands. Photons scattered three times all near $\theta = \frac{\pi}{2}$ similarly accumulate near lines corresponding to odd multiples of one half the bands' width. The extent of this effect for photons scattered more than twice is not as severe as it is for double scattering because there is a higher probability that one of the scattering events will be in a direction that is not near $\theta = \frac{\pi}{2}$, where the bands have different widths. Blindly sorting the photons into some other increments of solid angle generally results in some of the new increments covering more lines of doubly or triple scattered photons than others. This creates an artificial variation of the multiple scattering distribution with θ. We eliminated this by smearing; for each exiting photon a random number in the range ± half the width of the first band was added to the final value of θ.

Although the distribution of multiply scattered photons can be fit directly, the ratio of multiple to single scattering is of more physical interest. Experiments measure the total scattered intensity I_t, which contains contributions from both single and multiple scattering $I_t = I_s + I_m$. The single scattering can thus be deduced from the total and the ratio I_m/I_s as

$$I_s = \frac{I_t}{1 + I_m/I_s}. \tag{3.1}$$

For the geometry of Haller *et al.*, the single scattering can be computed as follows. If the simulation launches N photons, then the total number of photons N_0 that would have entered the cell in the incident beam is $N_0 = N/(1-e^{-2\tau R})$, where $2R$ is the path length of the incident beam in the cell. The number of photons singly scattered into one of the fitting bins covering the angular range $\theta_{\min} \leq \theta \leq \theta_{\max}$, $\varphi_{\min} \leq \varphi \leq \varphi_{\max}$, is accurately given by

$$N_1(\theta,\varphi) = N_0 e^{-\tau R} \int_{\varphi_{\min}}^{\varphi_{\max}} \int_{\theta_{\min}}^{\theta_{\max}} \frac{d\sigma}{d\Omega}(\theta,\varphi) \times \frac{w e^{-\tau R/\cos\theta}}{\sqrt{1-\sin^2\theta\,\cos^2\varphi}} \sin\theta\, d\theta\, d\varphi, \tag{3.2}$$

where w is the width of the slit image in the cell, which we have assumed to be small compared to R. Except at small scattering angles, $w/\sqrt{1-\sin^2\theta\,\cos^2\varphi}$ is the length of that portion of the beam from which single scattering satisfies the criterion of appearing to come from within the slit image. At small scattering angles, the entire length of the incident beam within the cell satisfies this criterion and this term must be replaced by $2R$.

Because I_s is very small near $\theta = 0$ and π, the ratio of multiple to single scattering may be fit over a large band of solid angle centered around $\theta = \frac{\pi}{2}$, which is the region of interest. We used the band defined by $\frac{\pi}{4} \leq \theta \leq \frac{3\pi}{4}$. Since the scattering process is symmetric about $\varphi = 0$, the average of the ratio at φ and $2\pi - \varphi$ was fit. After checking that the simulation indeed produced the same results for $\theta > \pi/2$ and $\theta < \pi/2$, these two regions were averaged together to further improve the statistics.

Figure 3 is a gray scale plot showing the number of

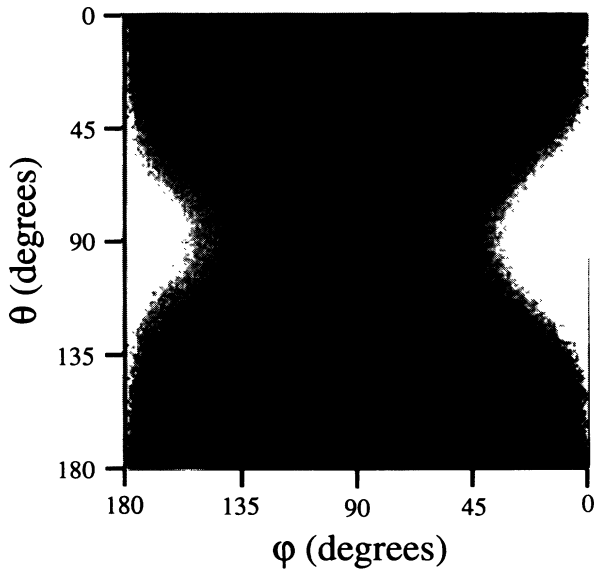

FIG. 3. A gray scale density plot of the number of accepted multiply scattered photons per unit solid angle as a function of θ and φ. White represents $\sim 10^7$ photons, while the gray areas in the center of the figure correspond to $\sim 10^5$ photons and black to zero photons per unit solid angle. The increments of solid angle used to produce the plot are 1° in each direction. This multiple scattering distribution resulted from an Ornstein-Zernike cross section with a correlation length of 1348 Å and $f_0 = 1.214$ cm^{-1} (see text). For this simulation about 6.4×10^8 photons were launched and 6.2×10^8 rescattered before leaving the sample. Of those that rescattered about 250 000 were ultimately accepted.

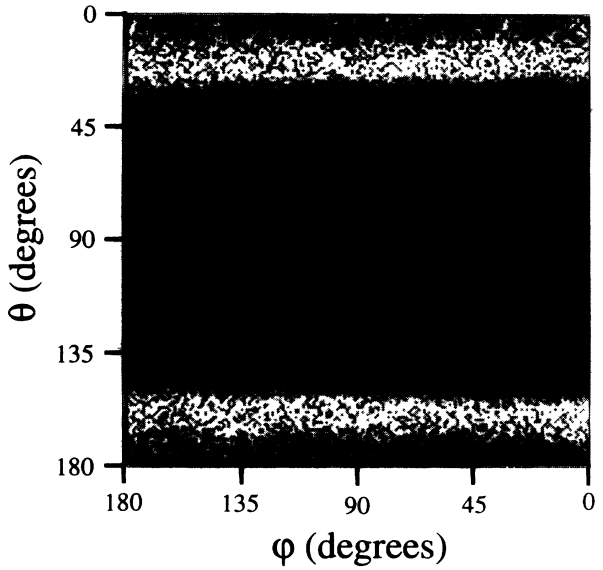

FIG. 4. A gray scale plot of the ratio of multiple to single scattering as a function of θ and φ for the same scattering cross section used to produce Fig. 3. Dark and light areas correspond to regions where the ratio is small and large, respectively. Black corresponds to a value of zero, while the gray near $\theta = 90°$, $\varphi = 135°$ corresponds to ~ 2. The very white and black areas near $\theta = 0°$ and 180° are the result of the single scattering decreasing to zero as the scattering direction approaches the polarization direction of the incident beam. Notice the uniformity of the density in the range $45° \leq \theta \leq 135°$.

accepted multiply scattered photons per unit solid angle as a function of the scattering direction for a particular simulation. It is apparent from the figure that there is a region around the entering and exiting beam for which the multiple scattering is particularly strong. This effect is similar to what is seen for single scattering in typical geometries. It arises because the length of the incident beam from which a slit will accept singly scattered light varies as $1/\sin\theta_s$, where θ_s is the scattering angle. For multiply scattered light, the effect is less pronounced because the multiply scattered light does not originate from such a narrow source; it appears to come from a diffuse region centered on the beam. Consequently, the ratio of multiple scattering to single scattering actually becomes rather small for large and small θ_s. This is evident in Fig. 4, which is a gray scale plot of the ratio of multiple to single scattering for the results of the same simulation shown in Fig. 3.

The fact that the scattering angles for which the multiple and single scattering begin to saturate near $\theta_s = 0°$ and 180° are different makes it difficult to fit the ratio of multiple to single scattering. The intensity of single scattering which is accepted saturates for θ_s values sufficiently small that the entire length of the beam within the cell is imaged within the slit. Similarly, as one goes to scattering angles near $\theta_s = 0°$ and 180°, the virtual channels eventually collect light from the entire length of the multiple scattering "halo" around the beam and at this point the multiple scattering tends to saturate. Because the single scattering does not saturate until a smaller angle is reached, the ratio of multiple to single scattering tends to drop rapidly near $\theta_s = 0°$ and 180°. For this reason, a fitting function that has an adjustable cutoff at small and large scattering angles was employed, namely,

$$f(\theta,\varphi) = \sum_{i,j=0}^{3} a_{ij}\theta^i\varphi^j \tanh\left[b_0^2(\theta_s - b_1)\right] \times \tanh\left[b_2^2(b_3 - \theta_s)\right]. \tag{3.3}$$

The scattering angle $\theta_s = \cos^{-1}(\sin\theta\cos\varphi)$. All of the a_{ij} and b_i were adjusted to optimize the fit. The two-dimensional cubic part of the fitting function was adequate to fit nearly all of the angular range of interest. Only the approximate ranges of $\theta_s \leq 15°$ and $\theta_s \geq 170°$ were not well described by the cubic equation. In those regions, where the ratio I_m/I_s changes rapidly, the two tanh functions serve as adjustable cutoffs to accomodate this behavior. The ratio of multiple to single scattering was fit using 1° increments in both θ and φ, with each increment weighted equally. Assuming the uncertainty in N_m to be $\sqrt{N_m}$, where N_m is the number of multiply scattered photons in solid angle increment being fit, and there to be no uncertainty in N_1 would imply that the correct weightings to use in fitting I_m/I_s would be N_1^2/N_m, but for the cases considered here the results were sufficiently insensitive to the weightings that we used equal weightings in practice. When fit to Eq. (3.3) the simulation results of Fig. 4 in the angular band $\frac{\pi}{4} \leq \theta \leq \frac{3\pi}{4}$ yielded a fractional deviation of 18% per increment, which was typical for all the results to be presented below. These deviations were dominated by the statistical fluctuations in the number of multiply scattered photons per increment.

The above treatment of multiple scattering for the apparatus of Haller *et al.* is presented as an example of the general problems involved in calculating multiple scattering for an apparatus that accepts very little of the scattered light. The same basic technique of applying a criterion to the exiting photons that mimics having collection channels over a significant range of solid angle and then fitting those results should work on most such optical geometries. Another development along these lines which would be well worth considering would be to allow the virtual channels to employ slits of various widths so as to sample photons from a longer region near the cell center. For scattering angles sufficiently away from 0° and 180° the ratio of multiple to single scattering is quite insensitive to the actual slit width and thus more information could be utilized in the fitting procedure. In fact, the apparatus of Haller *et al.* uses slits with image widths of 0.09 mm or 0.12 mm, depending on the scattering angle, and in the simulation we used virtual channels with a uniform slit image width of 0.10 mm. For the cross sections we have studied the effect of doubling the slit width was less than 2% for the ratio of multiple to single scattering over the angular range of the instrument and this is within the overall accuracy of the simulation results.

Some experimental setups do not discriminate against scattering based on its apparent spatial origin, but rather only on the basis of its scattering angle. In that case, estimating the ratio of multiple to single scattering is accomplished much more efficiently because essentially no photons are rejected once they have been propagated throughout the cell. Consequently, for such geometries the artifice of virtual channels is not required. For example, a common type of small angle light scattering apparatus uses a lens to map the light scattered at a given angle in the cell onto a circle, with larger scattering angles corresponding to larger circles. The light corresponding to a small range of circle diameters is then detected for each scattering channel. In this case, any photon that exits the cell will be accepted by some channel, regardless of how many times it has been scattered. Once all of the photons launched have been propagated throughout the cell, the integral in the appropriate analog of Eq. (3.2) can be evaluated over the acceptance solid angle of each of the channels to get the number of single scattered photons. The ratio of multiple to single scattering is then known for each detector.

IV. APPLICATIONS

A. Critical phenomena data

In this section the use of simulation as a tool for deducing single scattering cross sections in the presence of significant multiple scattering will be illustrated. We consider first the case of a binary mixture of 2,6-lutidine and water near its (inverted) consolute critical point, utilizing as data the results of measurements made with the photometer of Haller *et al.* In this case the scattered intensity becomes increasingly strong and is peaked more and more about a scattering angle of 0° as the critical point is approached. Independent data for the sample turbidity were also taken on the same sample and served as an invaluable aid in the correction process.

The mixture of 2,6-lutidine and water was prepared at the critical concentration and cleaned by filtration. It was contained in a cylindrical cell of inner diameter 17.2 mm. The instrument was calibrated using toluene as the reference standard for scattering angles in excess of 6°, which were free of stray elastically scattered light. The strongly temperature dependent, but nearly isotropic, scattering from the sample itself for $T_c - T \geq 1\,^{\circ}\mathrm{C}$ was used to calibrate the two smallest scattering angles relative to all other scattering angles. This yielded data for the q-dependent scattering cross section in absolute units for various values of the temperature T.

These data were fit to Eq. (2.3) with $\theta = 90°$ using the Ornstein-Zernike form for $f(q)$,

$$f(q) = \frac{f_0}{1 + q^2\xi^2}, \tag{4.1}$$

where ξ is the correlation length. The fit was weighted by the inverse square of the measured uncertainty in the data [11]. The quantity f_0 is proportional to the order parameter susceptibility $\chi = (\partial c/\partial\mu)_T$. Both χ and ξ are known to diverge at the critical point as $t^{-\gamma}$ and $t^{-\nu}$, respectively. Here the reduced temperature $t \equiv (T_c - T)/T_c$, where T_c is the critical temperature, and the theoretical values [12] for γ and ν are 1.240 and 0.632, respectively, both of which have been verified experimentally for many systems. Figure 5 shows the results deduced for f_0 from fitting the uncorrected data to the OZ form. The value of T_c used in plotting the data was that determined from fitting the corrected data for the susceptibility. When these values were fit to the form $f_0 = \Gamma t^{-\gamma}$, a value of 1.27 was found for γ. The results for the correlation length values obtained from fitting the uncorrected data are shown in Fig. 6, again using the same value of T_c. Clearly, the correlation length data are affected rather seriously, but, despite this, the individual fits of the scattered intensity are not nearly as bad as might be expected. Figure 7 shows $f^{-1}(q)$ vs q^2 for the data set taken closest to T_c, at $(T_c - T) = 12$ mK. Although the deviations from the fit to the OZ form are systematic, they could escape notice, especially if the data did not extend to sufficiently small values of q.

As mentioned above, the sample turbidity can be measured and serves as an absolutely invaluable consistency check. If the turbidity calculated by integrating the measured cross section is greater than the measured turbidity, multiple scattering is present. This is illustrated by the data of Fig. 8. The comparison shows that multiple scattering is already affecting the scattering data for values of $T_c - T$ as large as 0.1 °C.

Since the results for ξ are so strongly affected, while those for f_0 are much less so, an iterative scheme was used to correct the data for multiple scattering. For

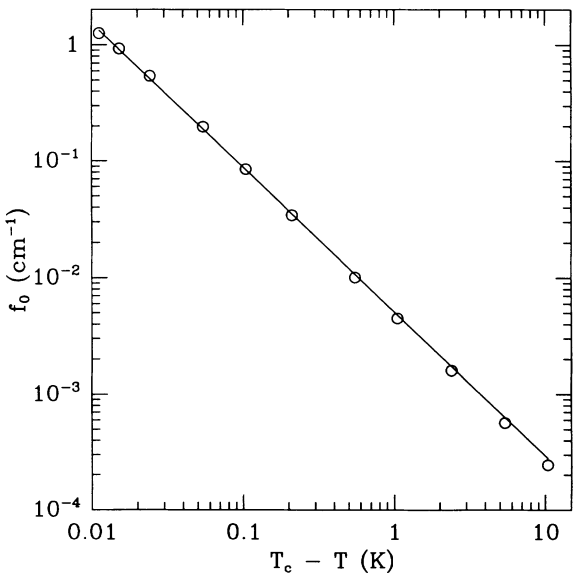

FIG. 5. Results for the $q = 0$ limit of the scattering cross section obtained by fitting uncorrected data to the Ornstein-Zernike form as a function of temperature difference from the critical temperature, for a sample of 2,6-lutidine and water. The line shows the theoretical asymptotic slope of −1.24.

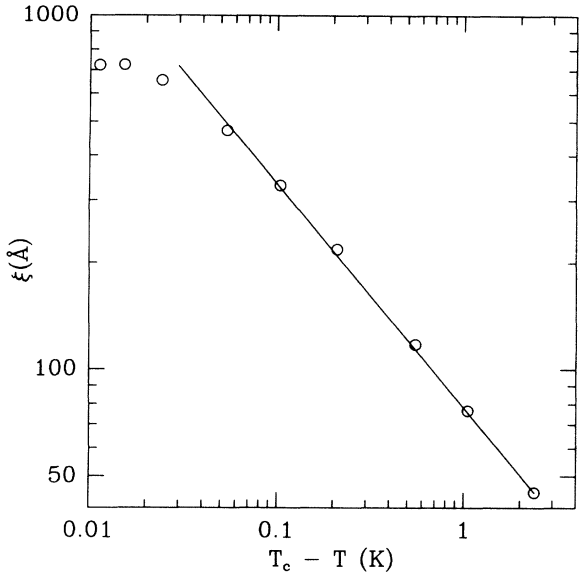

FIG. 6. Results for the correlation length obtained by fitting uncorrected data to the Ornstein-Zernike form vs temperature difference from the critical temperature. The solid line has a slope equal to the theoretical value of −0.63. Far from T_c the correlation length has roughly a power-law form, but near T_c it rolls off and apparently saturates as a consequence of multiple scattering.

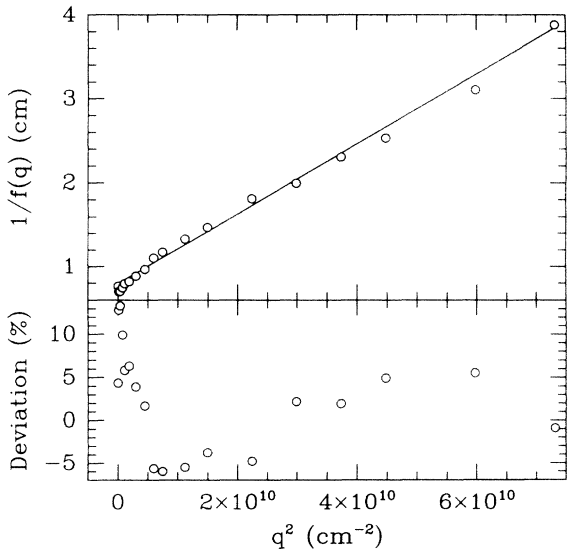

FIG. 7. An Ornstein-Zernike plot of the inverse of the scattered intensity vs q^2 for data taken 12 mK from the critical point. The solid line is a fit of the data to the Ornstein-Zernike form. As shown in the lower box, the deviations are large and systematic. If data were not available at small scattering angles, the deviations would be only ~ 5% or smaller, providing very little warning of the presence of strong multiple scattering.

each temperature, the measured τ, which is unaffected by multiple scattering, and the measured f_0 were used to deduce a trial value for ξ. The simulation was run with those values of f_0 and ξ and the resulting corrected data were then fit to determine a new f_0 and ξ. The parameters for subsequent iterations were chosen to lie between the fit results and the last values used for the simulation. The process was terminated when the fit results agreed with the previous simulation parameters to 0.5%. This required at most four iterations. As an example of the value of knowing the turbidity, we attempted to correct the data set taken closest to T_c using only f_0 and ξ found by fitting to the OZ form; after ten iterations the process had converged to within 2% of the f_0 and 1% of the correlation length found using the turbidity information.

After correction for multiple scattering, the data were again fit to the OZ form. The first obvious consequence was a considerable improvement in the fit for data taken near T_c as shown by the deviations from the fit before and after correction in Fig. 9. Clearly, the deviations are much less systematic for the corrected data. The reduced χ^2 parameter of the fit to the corrected data was 5.8, while fitting the uncorrected data yielded $\chi^2 = 29.5$.

The ratio of double to single scattering from the simulation for the data taken closest to T_c and the same ratio calculated using the method of Shanks and Sengers are compared in Fig. 10. The factor of $\sin\theta$ in Eq. (2.12) of Ref. [5], which is in error [13], was omitted in calculating the results for double scattering according to the method of Shanks and Sengers. The close agreement between the simulation results for double scattering and the calculated results gives confidence in the simulation. Also

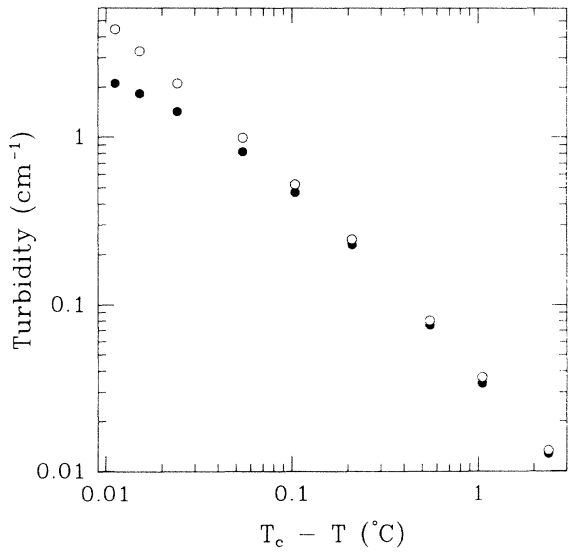

FIG. 8. A log-log plot of turbidity (integrated scattering cross section) vs temperature difference from the critical temperature. Closed symbols are measured values, which are not affected by multiple scattering, and the open symbols are values obtained from the measured angular distribution of the total scattered light intensity. Multiple scattering causes the values obtained from the scattering to exceed the true values by more than a factor of 2 for small $T_c - T$. A significant difference between the computed and measured turbidity is a reliable experimental indicator of the presence of multiple scattering.

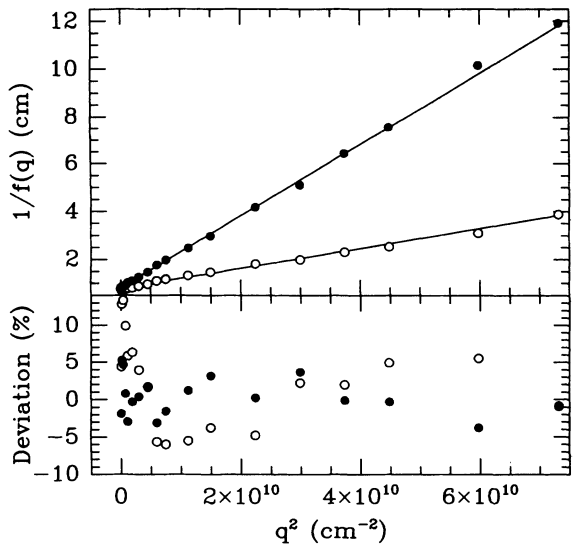

FIG. 9. An Ornstein-Zernike plot of the inverse of the scattered intensity vs q^2 for data taken 12 mK from T_c before (open symbols) and after (solid symbols) correcting for multiple scattering. Note that the correction made to the raw data was as large as a factor of 3 at large q^2. The lower portion of the figure shows the deviations between the data and the fit for both the uncorrected (open circles) and corrected (solid circles) data. The strong systematic deviations present for the uncorrected data are essentially eliminated by the correction.

shown in the figure is the ratio of multiple scattering to single scattering I_m/I_s from the same simulation. Probably the single most important feature to note is that the ratio I_m/I_s is less than 10% at a scattering angle of 2.7°, despite the fact that the ratio is over 2 at large angles. Physically, this is a result of the $1/\sin\theta_s$ dependence for the single scattering intensity accepted in this geometry, resulting in a strong increase in single scattering as θ_s approaches 0°. This is the fundamental reason why data taken with this instrument yield reasonably accurate values for f_0 even in the presence of severe multiple scattering. The $1/\sin\theta_s$ argument fails for angles near 180° because there are many paths whereby multiply scattered photons can be accepted without traversing distances as long as that covered by singly scattered photons in the sample causing severe multiple scattering in highly turbid samples.

Having corrected all the data taken within 0.25 K of T_c, results for f_0 and ξ vs $T_c - T$ are presented in Figs. 11 and 12, respectively. When the data for f_0 were fit to $f_0 = \Gamma t^{-\gamma}$ with Γ, γ, and T_c adjusted, the results were $\Gamma = (3.5 \pm 0.3) \times 10^{-6}$ cm^{-1} and $\gamma = 1.257 \pm 0.016$. The result for γ differs from the theoretical value by 1.4%. When a single Wegner term of the form $(1 + a_1 t^{\Delta})$ with $\Delta = 0.5$ was included, the fit improved substantially and gave $\Gamma = (3.9 \pm 0.3) \times 10^{-6}$ cm^{-1} and $\gamma = 1.243 \pm 0.012$, in excellent agreement with the theoretical value of 1.241. Inclusion of an additional Wegner term improved the fit somewhat and the best fit value of γ increased to 1.265 ± 0.023, still consistent with the theoretical value. A value of $T_c = 33.391$ °C was found independent of the number

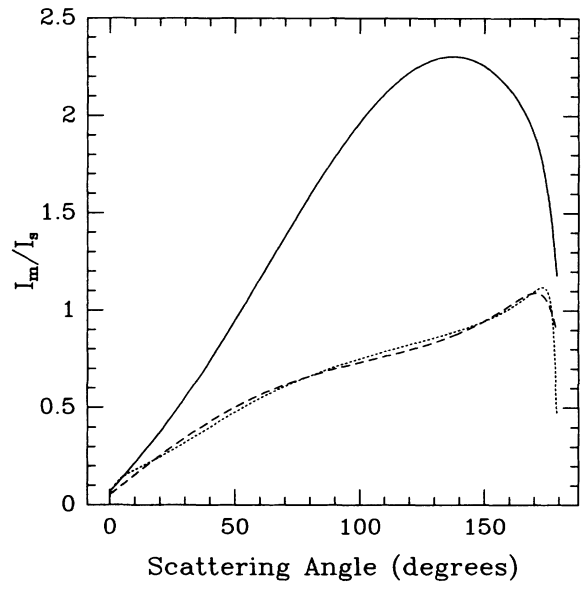

FIG. 10. Ratio of multiple to single scattering vs scattering angle for a single scattering cross section of the Ornstein-Zernike form with a correlation length of 1348 Å and $f_0 = 1.214$ cm^{-1} (solid line). The dashed line is the ratio of double scattering to single scattering from the same simulation, while the dotted line shows the ratio of double to single scattering calculated using the method of Shanks and Sengers for the same scattering cross section and optical geometry.

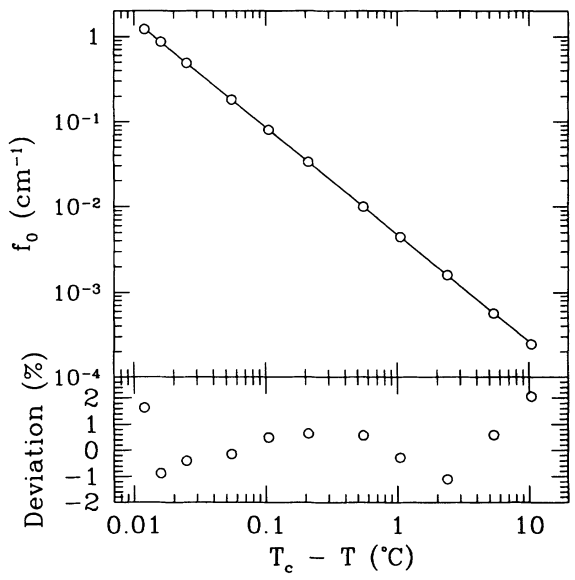

FIG. 11. The $q = 0$ limit of the scattering cross section obtained by fitting the corrected data to the Ornstein-Zernike form at each temperature as a function of $T_c - T$. The line is a fit to the data, including a single Wegner term, which yielded the value $\gamma = 1.243 \pm 0.012$ for the leading exponent. The lower portion of the figure shows the deviation of the data from the fit.

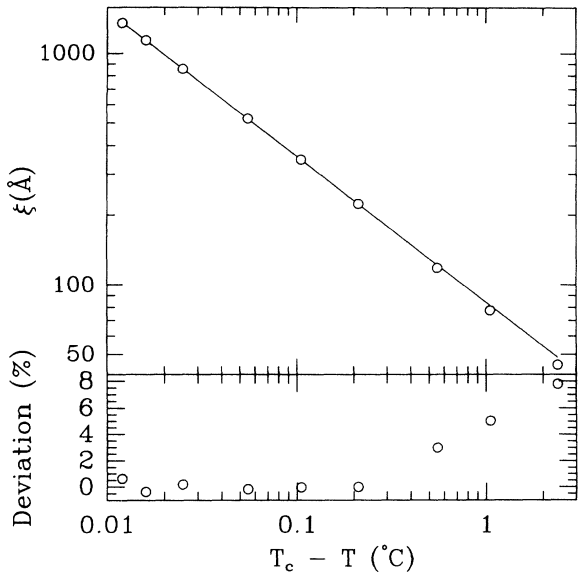

FIG. 12. Data for the correlation length as a function of $T_c - T$ obtained by fitting the corrected data to the Ornstein-Zernike form at each temperature. The line is a simple power-law fit to the data, which gave $\nu = 0.630 \pm 0.004$.

of Wegner terms.

The correlation length data, which are shown in Fig. 12, were fit to $\xi = \xi_0 t^{-\nu}$ with T_c fixed at the value above, which yielded $\xi_0 = 2.28 \pm 0.13$ Å and $\nu = 0.630 \pm 0.004$, in excellent agreement with theory. This fit is shown by the solid line in the figure. No Wegner terms were considered because of the limited temperature range for the correlation length data. Clearly, the original data were badly distorted by multiple scattering and yet the corrected data agree well with what is known about critical phenomena.

The turbidity calculated from the fit to the corrected data agreed with the measured turbidity to within 5% for all the data sets corrected. This is a remarkable improvement over the 220% difference found when comparing the turbidity calculated from the uncorrected scattering data to that measured 12 mK from T_c.

B. Spinodal decomposition data

We turn now to a discussion of a rather different scattering cross section using data that were obtained [14] in an optical geometry very different from that used for the measurements on lutidine and water. The data were taken during the process of spinodal decomposition for a sample of 3-methylpentane and nitroethane at the critical concentration. The sample was originally in the stable one-phase region above T_c and a sudden pressure drop was used to quench it into the unstable region lying below the coexistence curve. The optical geometry employed was again cylindrical, but with the incident beam passing along the axis rather than along a diameter. A lens of focal length f placed at the exit window served to map light scattered at an angle θ_s into a ring of radius $f \tan\theta_s$ lying in the focal plane of the lens. An array of 24 concentric circular detectors placed in the focal plane detected the scattered light whose scattering angle was in the range from 0.7° to 13.0°. Since this geometry discriminates scattering based only on angle and not position, it accepts essentially all single and multiply scattered light.

At first, it might seem hopeless to attempt to correct data where the scattering is known only over such a small angular range. In the present case, however, it proved feasible because the cross section is very small outside that range. Consequently, almost any reasonable approximation to the cross section in the region where data are not available is adequate. Of course, any cross section used must be consistent with the measured turbidity and, as was the case for critical scattering, this provided a very important constraint. The form we chose to use was

$$f(q) = Ae^{-bq^2}q^p[1 - C(q)] + \frac{B}{1 + q^4\xi^4}C(q) \qquad (4.2)$$

with

$$C(q) = \frac{1}{2}\{1 + \tanh[w(q - q_0)]\}. \qquad (4.3)$$

The first term generates a peak and the second term produces a power-law decay going as q^{-4} for large enough q. The data were corrected by fitting them to the form given by Eq. (4.2), adjusting A, b, p, w, q_0, B, and ξ. In this process the turbidity calculated from the fit was forced to agree with the measured turbidity, primarily by controlling B, ξ, and to some extent $C(q)$.

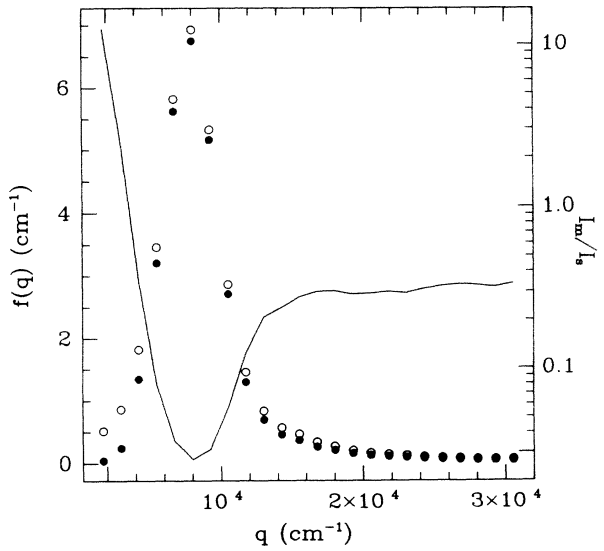

FIG. 13. Scattering cross section as a function of q, for a sample of 3-methylpentane and nitroethane undergoing spinodal decomposition. The data were taken 7.78 sec after making a quench 1.036 mK into the two-phase region. Uncorrected data are shown as open circles and the solid circles show the data after correction for multiple scattering. The scale of the data is given by the vertical axis on the left. The solid line is the ratio of multiple to single scattering as a function of q and refers to the logarithmic scale on the right.

The simulation was run using the fit cross section and the results were used to correct the data. The entire process was repeated until it converged, which required only two iterations. Figure 13 shows the results of the correction for one particular data set, taken 7.78 sec after initiating a quench to 1.036 mK below T_c. Although the correction is only of order 10% in the vicinity of the peak, it is very large near $q = 0$, where almost all of the scattering is multiple scattering. The single scattering lies essentially in a cone with its axis along the incident beam; rescattering of the single scattering will lie primarily on the surfaces of a set of cones whose axes lie on the original cone of single scattered light and these cones all intersect at $q = 0$, resulting in a high intensity of double scattering near $q = 0$.

V. SUMMARY

A practical method for the calculation of multiple scattering which works to all orders has been described. The important steps which make it possible to run the simulation on a workstation are the division of the incident beam into equal probability sections, the binning of all solid angle into increments of equal scattering probability, and the use of virtual scattering channels when necessary. The solid angle binning allows one to handle all scattering processes in an identical manner and the selection of scattering angles is reduced to choosing a random number and selecting the scattering angle from a look-up table. Furthermore, since the calculation of the proper solid angle binning utilizes a small fraction of the total simulation time, this method should be equally applicable to more complicated scattering cross sections, such as Mie scattering, scattering from particles in the atmosphere, etc. The same method should be useful in neutron scattering as well. In fact, since small angle neutron scattering setups do not discriminate against neutrons based on where they appear to have been scattered, but only upon their scattering angle, simulation should be very efficient.

The simulation was able to correct data taken near the consolute point of the 2,6-lutidine and water mixture. We are confident of the accuracy of the corrections since the double scattering corrections agree with the calculations of Shanks and Sengers and the corrected data set gives accurate power-law behavior for both the correlation length and susceptibility, with exponents in good agreement with known values. The multiple scattering correction of the spinodal decomposition data represents a less well-defined problem in that the true scattering cross section is not known over a significant range of q values. Even so, the corrections were consistent with our expectations and self-consistent in that the correction process converged within two iterations.

The amount of computer time required for these two different problems was radically different because of the amount of scattered light accepted by the two different apparatus. All simulations were run using a 68040 based NeXT computer. The critical phenomena corrections for a typical data set typically involved tracking $\sim 10^9$ photons and required about 5 days and the spinodal decomposition corrections tracking $\sim 5 \times 10^7$ photons required about 5 h per data set.

The distribution of initial launch points of the photons acceptable to the virtual detectors appropriate to the Haller *et al.* apparatus was found to be highly peaked in the vicinity of the center of the cell. For the cross section appropriate to the 2,6-lutidine and water sample 12 mK from T_c, 19% of all the acceptable multiply scattered photons originate within 0.5 mm of the center of the cell. Because of this effect, a simulation with four times as many beam sections was performed to ensure the invariance of the results with respect to beam section density. The ratio of multiple to single scattering differed by no more than 2% from the original result. Similarly, simulations were performed with both four times more and four times fewer directional bins for this same cross section. Neither simulation showed more than a 3% deviation from the original ratio of multiple to single scattering. Decreasing the density of directional bins resulted in a slightly larger change than increasing the density.

Naively, one might think that multiple scattering processes where photons reflected at or near grazing incidence from either the inner or outer cell wall might affect the multiple scattering distribution. On this assumption, we included in the simulation the possibility of reflections from the cell walls in the correction of the data taken 12 mK from T_c for the 2,6-lutidine and water mixture. The reflections changed the ratio of multiple to single scattering by less than 3% at all angles and the values of f_0 and ξ found from the corrected data by less than 0.3%. Including the reflections increased the required computation time by roughly a factor of 2; therefore, since they have a small effect, reflections were not included in the analysis of the data.

The question of how to know when multiple scattering is affecting data is a difficult one. The effect is dependent on both the optical geometry and the scattering cross section. Probably the best way to answer this question is to measure the turbidity and compare it to the turbidity found by fitting the scattering data and integrating over all solid angle. Without knowledge of the turbidity, only running a simulation such as the one described here is likely to give an accurate indication of the importance of multiple scattering.

The approach developed here could be generalized in several ways. For example, the incident beam was treated as a line, but in practice it has a finite width, which should be easy to simulate. Since the simulation yields the polarization state of every exiting photon, calculation of the depolarization ratio should also be straightforward. There is no particular reason that the cross section should be restricted to the simple Rayleigh forms considered here, nor is the assumption of fully polarized single scattering in any way essential.

We have not attempted to generalize the method for use with dynamic light scattering. There are some rather subtle effects that would have to be treated carefully to do so. Single scattering originates from the diffraction limited focal region of a laser in the typical dynamic light scattering setup. The single scattered light has a

significant degree of spatial coherence as a consequence. Multiple scattering originates from a larger region with a depth that is usually comparable to the sample dimension. Consequently it will have different spatial coherence properties; specifically it will be spatially coherent to a lesser degree than single scattering. For this reason it will contribute less to the power spectrum or correlation function of the fluctuations in the detector output for any channel that accepts light over a finite acceptance solid angle. In addition, the scattered field that is being rescattered to generate the double and higher-order scattering has spatial coherence properties that depend on position within the sample and this can affect the temporal correlation properties of the rescattered light [15].

ACKNOWLEDGMENTS

We thank Dr. Joseph Shanks for providing us with the computer code to calculate the analytic double scattering described by Shanks and Sengers. We also thank B. J. Frisken for her help in checking both the theory and the computer code for the method of Shanks and Sengers. The work reported here was supported by Grant No. NSF DMR90-18089.

[1] D.W. Oxtoby and W.M. Gelbart, Phys. Rev. A **10**, 738 (1974).
[2] D.W. Oxtoby and W.M. Gelbart, J. Chem. Phys. **60**, 3359 (1974).
[3] L.A. Reith and H.L. Swinney, Phys. Rev. A **12**, 1094 (1975).
[4] A.J. Bray and R.F. Chang, Phys. Rev. A **12**, 2594 (1975).
[5] J.G. Shanks and J.V. Sengers, Phys. Rev. A **38**, 885 (1988).
[6] M.E. Fisher and R.J. Burford, Phys. Rev. **156**, 583 (1967).
[7] J. Felsteiner, P. Pattison, and M. Cooper, Philos. Mag. **30**, 537 (1974).
[8] V. Halonen and B. Williams, Phys. Rev. B **19**, 1990 (1978).
[9] R. Seriman, T. Pitkänen, S. Vahuaselkä, and T. Paakkari, J. Appl. Cryst. **23**, 11 (1990).
[10] H.R. Haller, C. Destor, and D.S. Cannell, Rev. Sci. Instrum. **54**, 973 (1983).
[11] Unless stated otherwise, data, or parameters already deduced by fitting data, were weighted by the inverse of the squares in their uncertainties when they were being fitted.
[12] M.E. Fisher and J.-H. Chen, J. Phys. (Paris) **46**, 1645 (1985).
[13] B.J. Frisken, F. Ferri, and D.S. Cannell, Phys. Rev. Lett. **66**, 2754 (1991).
[14] A.E. Bailey and D.S. Cannell, Phys. Rev. Lett. **70**, 2110 (1993).
[15] D.M. Kim, J.G. Gallagher, Jr., and C.D. Armeniades, Phys. Rev. Lett. **39**, 804 (1977).

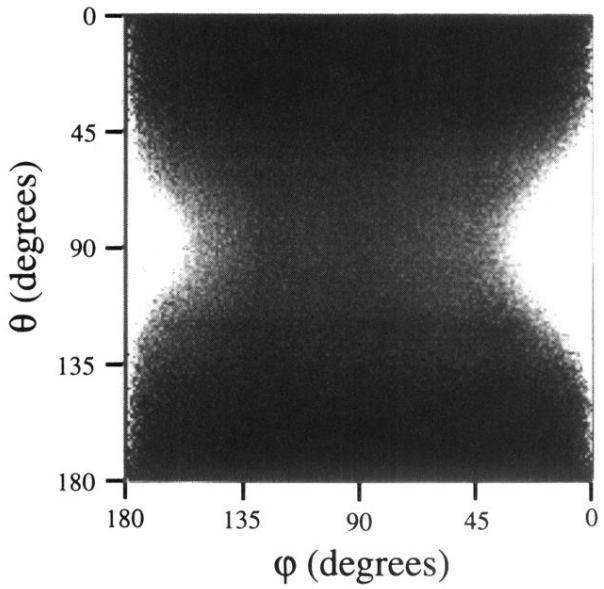

FIG. 3. A gray scale density plot of the number of accepted multiply scattered photons per unit solid angle as a function of θ and φ. White represents $\sim 10^7$ photons, while the gray areas in the center of the figure correspond to $\sim 10^5$ photons and black to zero photons per unit solid angle. The increments of solid angle used to produce the plot are 1° in each direction. This multiple scattering distribution resulted from an Ornstein-Zernike cross section with a correlation length of 1348 Å and $f_0 = 1.214$ cm^{-1} (see text). For this simulation about 6.4×10^8 photons were launched and 6.2×10^8 rescattered before leaving the sample. Of those that rescattered about 250 000 were ultimately accepted.

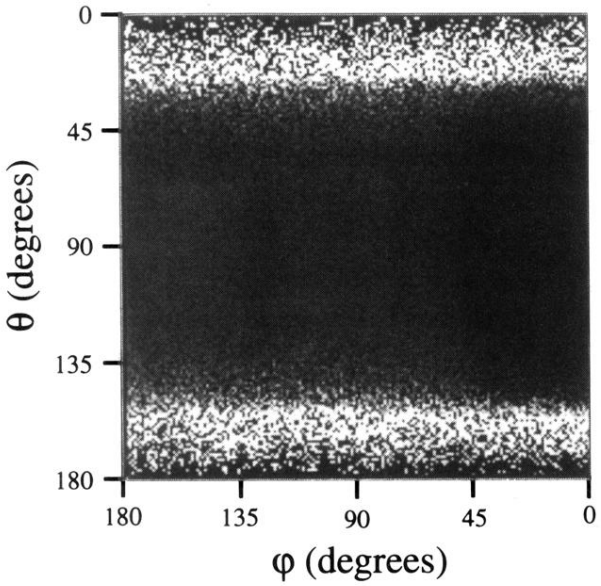

FIG. 4. A gray scale plot of the ratio of multiple to single scattering as a function of θ and φ for the same scattering cross section used to produce Fig. 3. Dark and light areas correspond to regions where the ratio is small and large, respectively. Black corresponds to a value of zero, while the gray near $\theta = 90^\circ$, $\varphi = 135^\circ$ corresponds to ~ 2. The very white and black areas near $\theta = 0^\circ$ and 180° are the result of the single scattering decreasing to zero as the scattering direction approaches the polarization direction of the incident beam. Notice the uniformity of the density in the range $45^\circ \leq \theta \leq 135^\circ$.